ChemComm

HIGHLIGHT

View Article Online
View Journal | View Issue

Cite this: *Chem. Commun.*, 2024, **60**, 14703

Soft optical materials based on the integration of perovskite nanostructures and block copolymers

Naifu Shen, Jinyu Bu, Xun Liu and Weinan Xu *

Metal halide perovskites and their nanostructures have efficient optical absorption and emission in the visible range with high external quantum efficiency. They have been at the forefront of next-generation photovoltaics and optoelectronics applications. But several intrinsic limitations of perovskites including low stability and incompatibility with lithography-based patterning constrains their broader applications. In recent years, the integration of perovskites with polymers especially multifunctional block copolymers (BCPs) has provided a new approach to overcome those issues. The chemical composition and chain architecture of BCPs are critical for achieving synergistic effects with perovskites in their hybrid systems. In this Highlight review article, we provide an overview and critical summary of the recent progress in the creation of perovskite–BCP hybrid structures, with a focus on the different roles of BCPs. The major categories include: (i) BCPs act as the nanopattern template for the spatial control and patterning of perovskite; (ii) BCP micelles or stars act as the template for perovskite nanostructure crystallization; (iii) BCPs act as the macromolecular ligands for perovskite NCs during its solution synthesis; (iv) BCP encapsulation of perovskite NCs into hierarchical composite particles; and (v) BCP incorporation into bulk perovskite and forming bulk composite films. The applications of perovskite–BCP hybrid structures in various fields and the major current challenges are also identified and discussed.

Received 1st October 2024,
Accepted 22nd November 2024

DOI: 10.1039/d4cc05181e

rsc.li/chemcomm

School of Polymer Science and Polymer Engineering, The University of Akron, Akron, OH 44325, USA. E-mail: weinanxu@uakron.edu

Weinan Xu

Dr Weinan Xu is an assistant professor in the School of Polymer Science and Polymer Engineering at the University of Akron since 2019. He obtained his PhD degree in Materials Science and Engineering from Georgia Institute of Technology and did postdoctoral research at Johns Hopkins University. His current research is focused on the development of functional/sustainable polymer nanocomposites and their advanced manufacturing, with applications in electronics, biomedicine, and energy storage. He has been recognized with several awards, including the DARPA Young Faculty Award, Polymer Processing Society Early Career Award, and Best PhD Thesis Award from Sigma Xi and Georgia Tech.

1. Introduction

Perovskites, or more specifically, metal halide perovskites (MHPs), are a type of semiconducting materials with unique optical and electronic properties.[1,2] They have been at the forefront of photovoltaics and optoelectronics research due to their efficient optical absorption and emission in the visible range.[3,4] MHPs generally have a ABX_3 crystalline structure where the organic or inorganic cations (such as MA: $CH_3NH_3^+$, FA: $CH(NH_2)_2^+$, or Cs^+) occupy the voids (A sites) created by eight corner-sharing BX_6 (B is bivalent cation and X is halide anion) octahedron.[4,5]

MHPs possess direct or indirect bandgaps and high joint density of states, they generally have more efficient light-absorbing capability compared with conventional semiconductors. The tunable bandgap *via* halide exchange reaction and exciton dissociation through radiative recombination enable their light-emitting capabilities with a wide color gamut. Another advantage of MHPs as a semiconductor is their intrinsic defect tolerance.[6] Mid-gap trap states due to interstitial or antisite defects are difficult to form in MHPs due to the large formation energy. Vacancy defects with low formation energy only create shallow trap states near the bandgap edges,[7] which cannot dramatically alter the perovskite's electronic structure. The efficient photoelectric conversion and efficient charge transport property of MHPs also make them suitable for photocatalytic applications.

MHPs can be synthesized and used in bulk state or in the form of nanoparticles and quantum dots (QDs). Compared to their bulk crystal counterpart, perovskite QDs have a discrete, size-dependent bandgap structure[8] due to the quantum confinement effect. A blueshift in the emission spectrum will take place as the size of QDs gets smaller towards free electron's de Broglie wavelength.[9] Due to the restricted electron and hole wavefunction, a sharp DOS appears and leads to narrow optical emission as well as high color purity. Moreover, perovskite QDs can reach near-unity PL quantum yield with highly tunable emission colors.[10–12] Therefore, perovskite QDs are more and more used for next-generation display and optoelectronic applications.

Bulk halide perovskite is often deposited as thin films using a solution-based one-step procedure where the crystal growth is controlled by antisolvent-dripping[13] or Lewis acid–base adduct formation.[14] Perovskite QDs are usually synthesized by hot injection method,[15] or ligand assisted reprecipitation (LARP).[16] The LARP method is usually conducted by dissolving the perovskite precursors and organic ligands in a nonpolar solvent, followed by dropwise injecting into a vigorously stirring bad solvent. All-inorganic perovskite QDs are usually synthesized by the hot-injection method, for instance, Cs-oleate hot solution is injected into halide precursors. The majority of the QDs formation takes place within a few seconds after the fast injection and thus size control of QDs is achieved by varying the reaction temperature or incorporating alkylammonium halide during the synthesis.[17]

Despite the advantages and desirable properties of perovskites and their nanostructures, there are two main limitations that constrain their broader applications. Firstly, MHPs generally have limited stability and are vulnerable to many environmental factors, including moisture, certain solvents, oxygen, and heat.[18–20] Perovskite QDs with high surface areas are more susceptible to the effects of the environment. Secondly, direct patterning of solid perovskite materials with photolithography-based techniques is not feasible due to the poor stability of perovskite under moisture, solvents, and dry etching.[21] The lack of efficient nanopatterning methods prevents their further development and applications.[22] Other nanopatterning techniques such as direct laser writing and focused ion beam milling have been explored for perovskites,[23,24] but those methods are time-consuming, costly, and difficult to scale up.

The integration of perovskite nanostructures with polymers emerges as a promising approach to address the above-mentioned challenges. The polymeric component has the potential to enhance the stability of perovskites by encapsulation or surface passivation.[25] It can also substantially improve the processability of perovskites with the utilization of versatile polymer processing technologies.[26,27] But simple blending of homopolymers with perovskite nanostructures will result in composite with uncontrolled aggregation and unsatisfactory physical properties due to the lack of specific interaction and precise structural control.

To address those issues in perovskite-polymer hybrid materials, block copolymers (BCPs) emerge as a functional platform to be integrated with perovskite nanostructures with enhanced properties and structural control.[28–30] BCP is defined as a type of polymers composed of two or more types of blocks, and the chemically bonded neighboring blocks have different chemical compositions or repeating units. In contrast to the physical mixing of incompatible homopolymers, which leads to macroscopic phase separation, BCPs adopt extended configurations to separate covalently bonded dissimilar blocks.[31] The chain stretching produces an entropic contribution that counteracts the driving force for separation, thereby constraining the phase separation to nanometer scale.[32]

The Flory-Huggin's interaction parameter χ_{AB} for two different blocks A and B in BCPs can be calculated by the following equation: $\chi_{AB} = \frac{Z}{k_B T}\left[\varepsilon_{AB} - \frac{1}{2}(\varepsilon_{AA} + \varepsilon_{BB})\right]$, where Z is the number of nearest neighboring monomers in a copolymer, k_B is the Boltzmann constant, and ε_{AB} is the interaction energy between A and B repeating units.[33] Positive χ_{AB} indicates repulsive interaction between A and B repeating units and negative χ_{AB} indicates a tendency towards mixing. Without strong interactions including hydrogen bonding or ionic interaction, χ_{AB} is usually a small and positive value, and varies inversely with temperature.[34]

Based on self-consistent mean-field theory,[35] the morphological evolution for BCP mainly depends on two parameters: (1) incompatibility degree, which is the product of χ_{AB} and the degree of polymerization N, (2) volume fraction of the building blocks. BCPs tend to form ordered microphase separation when χ^N is larger than a critical value. Different morphologies are formed in a manner that can minimize the interfacial energy which reflects the enthalpic contribution and simultaneously reduce chain stretching to provide highest configuration entropy possible to the system. Those morphologies include body-centered cubic spheres, hexagonally packed cylinders, bicontinuous gyroids, and lamellae, which can be controlled by varying the molecular weights, block ratios, processing conditions, and substrates.[35,36]

By designing the molecular structure and properties, BCPs have the potential to improve the stability of perovskite nanostructures by encapsulating them in a highly stable and soft matrix.[37] On the other hand, the microphase-separated BCP matrix makes it possible to achieve molecular-level control of the alignment and assembly of perovskite nanostructures.[38–40] Moreover, the versatility in chemical structures and architectures of BCP enables the synergistic integration of multiple functionalities for enhancing the properties of perovskite nanostructures. There is important recent progress in this specific topic of integrating perovskite with BCPs for the creation of soft functional optical materials and devices. This Highlight article aims to summarize those recent advancements in a logical and concise manner based on the versatile roles of BCPs in such hybrid optical materials.

We identified the following major categories of perovskite–BCP hybrid structures based on the different roles of BCP in the system (Fig. 1). First, the microphase-separated morphology of BCP provides an efficient method of nanopatterning of perovskite materials. This can be further divided into two methods: *in situ* formation of perovskite nanocrystals (NCs) from their precursors inside BCP template; or the directed assembly of perovskite NCs inside the BCP matrix. Second, BCP micelles or star-shaped BCP act as the template for

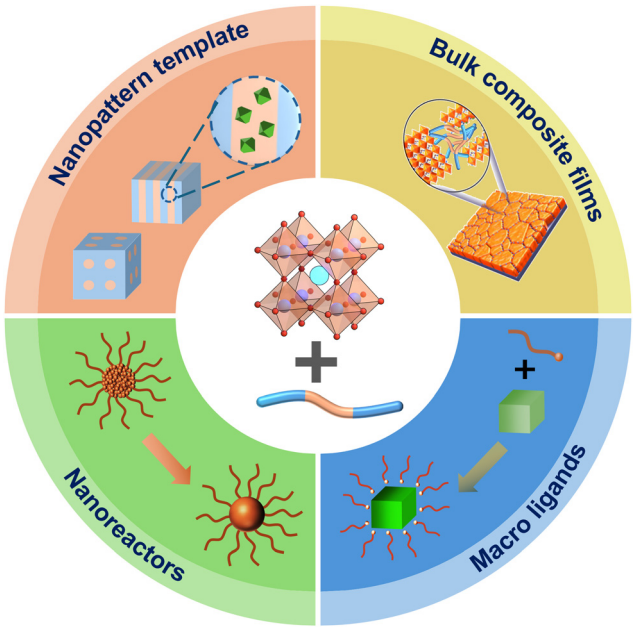

Fig. 1 Overview of the different roles of BCP in perovskite–BCP hybrid structures.

perovskite crystallization and form hybrid nanostructures. Third, BCP acts as the macromolecular ligands for perovskite NCs during its solution synthesis. Fourth, BCP encapsulation of perovskite NCs into hierarchical composite particles. Fifth, BCP is blended with perovskite and forms bulk composite films. We also summarized the representative applications of such perovskite–BCP hybrid structures in optics and photonics. In the end, we also discussed the remaining challenges of this field and the potential further research directions.

2. Perovskite–BCP hybrid structures

2.1 BCP as nanopattern template for perovskites

Nanopatterning of perovskites is critical for their advanced applications in optics and photonic devices. Due to the capability to form well-defined microphase-separated morphology of BCPs in nanometer scale, they provide a scalable and low-cost approach for nanopatterning of perovskite. This can potentially be achieved *via* two different approaches: (1) *in situ* formation of perovskite nanocrystals from their precursors within the BCP template; (2) directed assembly of perovskite nanocrystals within the microphase-separated BCP matrix.

2.1.1 *In situ* formation of perovskite NCs within BCP template. In order to achieve the *in situ* formation of perovskite NCs within BCP template, at least one of the blocks on BCP needs to have favorable or preferential interaction with perovskite precursors. The most common approach is by selecting BCPs with functional groups such as pyridine ring, carbonyl, or carboxyl group that can have electrostatic or Lewis acid–base interaction with the cationic ions on perovskites or their precursors. The accumulation of perovskite precursors around selective blocks of BCP and their subsequent crystallization enables the generation of spatially defined perovskite NCs.

For instance, the precursor solution (MABr and $PbBr_2$) of methylammonium lead halide ($MAPbX_3$, X = Br^-, I^-) perovskite was mixed with poly(styrene)-*block*-poly(2-vinylpyridine) (PS-*b*-P2VP),[41] and the mixture was spin-coated on a substrate (Fig. 2a). The obtained thin hybrid films showed well-defined patterns including cylinders, lamellae, and cylindrical mesh, with controlled domain size (40–72 nm) (Fig. 2b–d). The hybrid structures showed enhanced exciton recombination and longer exciton lifetime due to the reduced crystal size as well as the passivating effect of the P2VP phase that reduced surface defects on the perovskite. Excellent heat and moisture resistance of such hybrid structures was also demonstrated. In another report by the same group,[42] the nanopatterned hybrid structures composed of $MAPbBr_3$ perovskite and PS-*b*-P2VP were used as the main component for artificial photonic synapses or photoreceptor cells for information storage and learning applications. The microphase-separated morphology and the $MAPbBr_3$ density were spatially tuned to stimulate the rod and cone cells distribution in the visual perception system.

Using a similar strategy, perovskite precursors (MABr and $PbBr_2$) were mixed with polystyrene-*block*-poly(ethylene oxide) (PS-*b*-PEO) copolymers to form hybrid thin films (Fig. 2e),[43] and well-defined spatial pattern of the perovskite nanocrystals was achieved (Fig. 2f–g). The chelation between the lead ion and PEO segment promoted the anti-solvent functionalities of the hybrid films. Such perovskite/PS-*b*-PEO hybrid films were used as photoactive floating gate to elucidate the effect of morphology on the photo-responsive characteristics of photomemory. In another report,[45] they used a similar method to fabricate quasi-2D $FAPbBr_3$/PS-*b*-PEO hybrid films and used them as photoactive floating gate for flash photomemory devices with high performance.

In another recent study,[30] Ruddlesden–Popper perovskites/BCP hybrid structures were prepared by mixing the precursors of phenylethylene methylammonium lead bromide ($PEA_2MA_{n-1}Pb_nBr_{2n+1}$, n = 2, 3) and PS-*b*-PEO, followed by thermal annealing and crystallization. The perovskite crystals were geometrically confined within the microphase segregated BCP nanopatterns, the interaction between the Pb^{2+} ions of perovskite and the oxygen atoms of PEO in BCP resulted in both enhanced phase purity and ordered crystallization. Hung *et al.* demonstrated stretchable photonic device fabrication based on triblock copolymer maltoheptaose-*block*-polyisoprene-*block*-maltoheptaose (MH-*b*-PI-*b*-MH),[39] which provided a spatially confined environment for the crystallization of cesium lead halide ($CsPbX_3$) perovskite NCs. Such selective distribution was attributed to the coordination between the hydroxyl groups of the MH segment and the Pb^{2+} ions in the perovskite precursor. In another recent report,[46] PS-*b*-P2VP was assembled into alternating in-plane lamellae structure and showed structural color. By synthesizing $CsPbX_3$ or $MAPbX_3$ NCs inside the BCP *via* a two-step solution process, dual mode structure color and photoluminescent were demonstrated, which enabled encryption and decryption of sophisticated information.

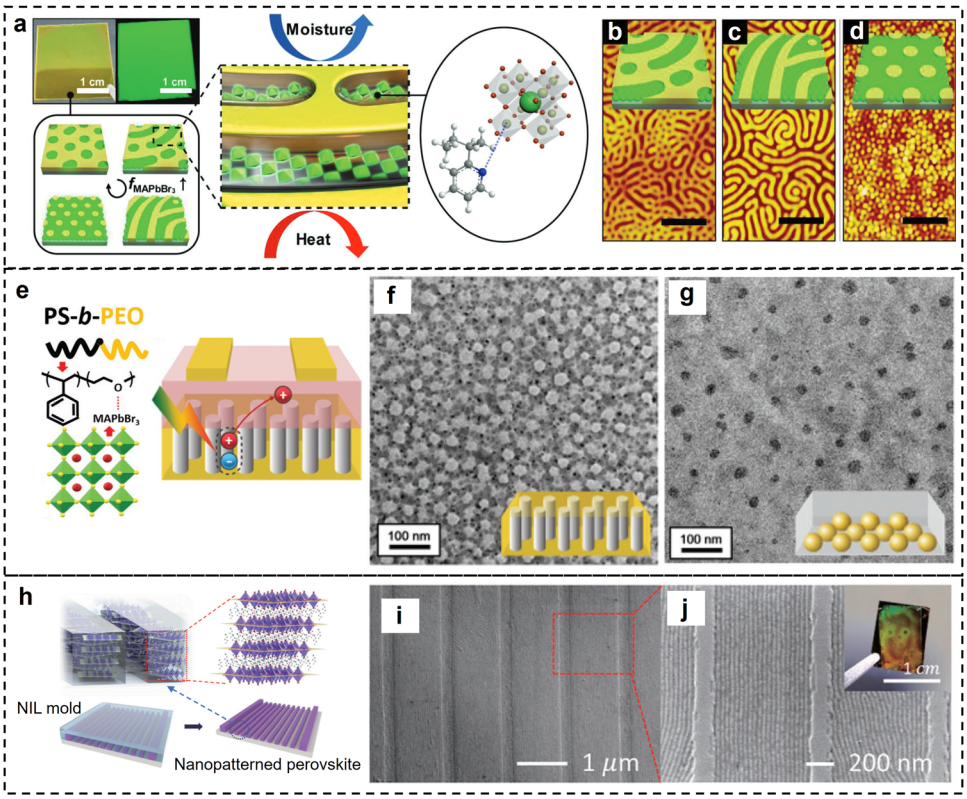

Fig. 2 (a) Schematic of the fabrication of nanostructured perovskite thin films templated with PS-*b*-P2VP self-assembly. (b)–(d) AFM images of the PS-*b*-P2VP/$MAPbBr_3$ nanostructured films (Mn = 125 kg mol^{-1}, f_{P2VP} = 0.32) with (b) 40%, (c) 60%, and (d) 100% $MAPbBr_3$. The scale bars are 500 nm. Reproduced with permission from ref. 41. Copyright 2019 Wiley-VCH. (e) Schematic of the Lewis acid–base interaction between PS-*b*-PEO and $MAPbBr_3$ perovskite, and the charge transfer process in the BCP/$MAPbBr_3$ composite films in the photomemory device. (f)–(g) TEM images of (f) symmetric PS-*b*-PEO/$MAPbBr_3$ and (g) asymmetric BCP/$MAPbBr_3$ composite films after solvent vapor annealing. Reproduced with permission from ref. 43. Copyright 2020 Wiley-VCH. (h) Schematic of the fabrication of nanopatterned 2D perovskites by NIL with a PS-*b*-PDMS derived mold. (i)–(j) SEM images of the BA_2PbBr_4 nanopatterns produced by this method. Reproduced with permission from ref. 44. Copyright 2023 Wiley-VCH.

On the other hand, the microphase-separated morphology of BCP can be used as the template for nanoimprinting lithography, which provides another method of nanopatterning of perovskites. For instance, PS-*b*-PDMS was self-assembled on a pre-patterned Si substrate to form well-defined nanopatterns with PDMS cylinders (thickness ≈30 nm) embedded in the PS matrix,[44] and the BCP pattern was then used for the fabrication of nanopatterned PDMS stamps (Fig. 2h). Subsequent nanoimprinting of the precursor film of a 2D perovskite ($A'_2MA_{n-1}Pb_nX_{3n+1}$, A′ = BA, PEA, X = Br, I) using the PDMS stamp resulted in well-defined 1D patterns of those 2D perovskites (Fig. 2i–j). Such nanopatterned 2D perovskites showed enhanced photoluminescence (PL) quantum yields (about four times higher) than those of the corresponding control flat films. In another report,[47] nanoimprinting guided self-assembly was conducted to fabricate nanopatterned hybrid perovskite structures. The two-step method consisted of spin-coating a mixture of the $MAPbBr_3$ precursors and PS-*b*-P2VP on the substrate followed by nanoimprinting. The P2VP block passivated the QDs surface through Lewis acid–base interaction and the nanopatterning provided local-field enhancement induced by Mie resonance, both contributing to the enhanced photoluminescence and stability.

2.1.2 Directed assembly of perovskite NCs with BCP matrix. The second approach to achieving nanopatterning of perovskites with BCP is through the directed assembly of perovskite NCs within the BCP matrix. In order to achieve precise control of the internal structure and interfaces in the perovskite–BCP composites, a selective block of the BCP needs to have preferential interaction with the organic or polymeric ligands on perovskite NC surface. In our recent work,[48] we designed and synthesized polyisobutylene (PIB)-based polymer ligands for $CsPbBr_3$ QDs, and based on the strong and selective interactions between the polymer ligands and polystyrene-*b*-polyisobutylene-*b*-polystyrene (SIBS) copolymer (Fig. 3a), a series of functional nanocomposites were prepared and their structure–property relationship was elucidated. We discovered that the chemical compatibility of the polymer ligands and copolymer matrix is the key to achieve precise control of the distribution of perovskite QDs inside the soft matrix and prevent aggregation (Fig. 3b). Moreover, the PIB-based ligands on perovskite QDs and the incorporation of p-QDs inside the PIB domain of SIBS copolymer can substantially enhance the PL stability due to the high impermeability and chemical stability of PIB. Such QDs/SIBS composites have excellent flexibility, stretchability and photoluminescent properties (Fig. 3c and d), which can potentially be used for flexible optoelectronics, optical storage, and displays.

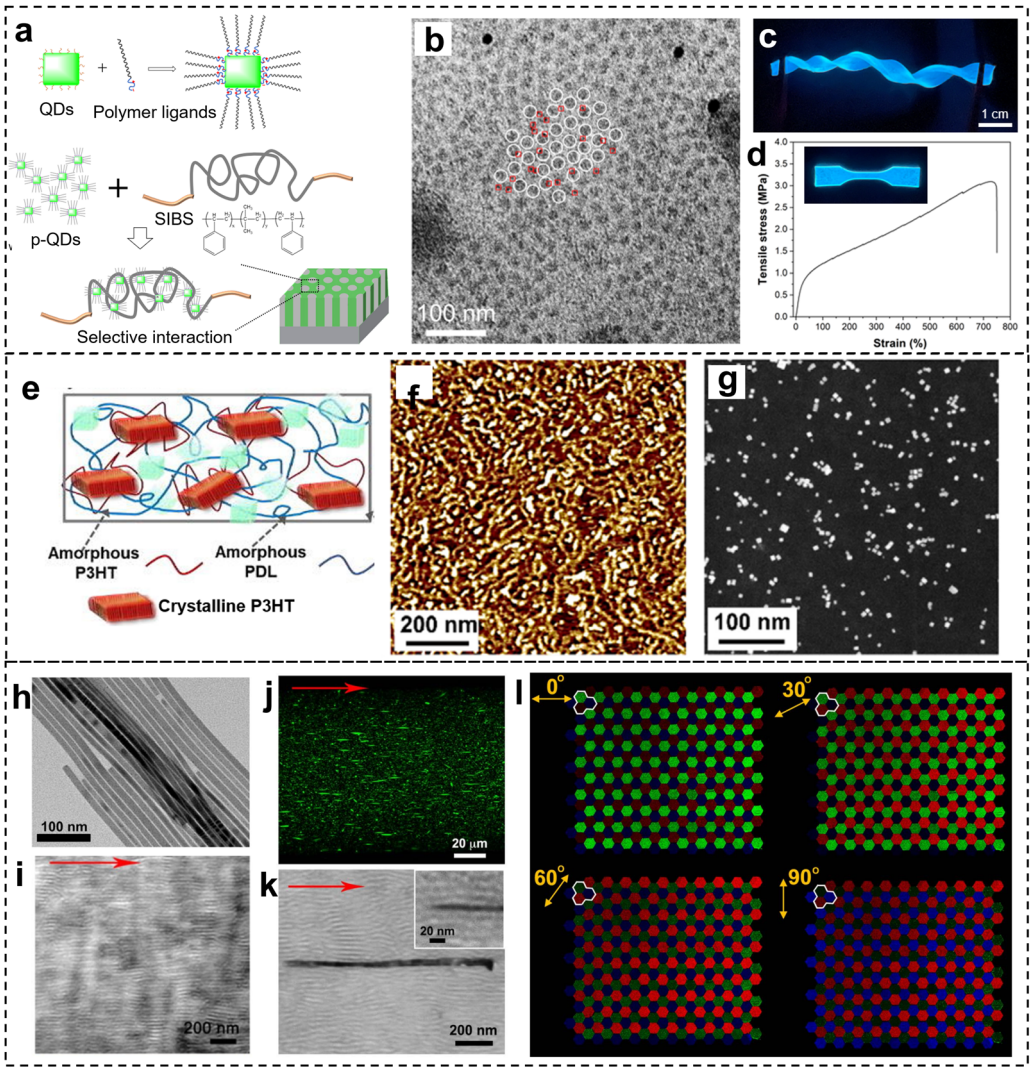

Fig. 3 (a) Schematic of the selective interaction between PIB-ligand functionalized $CsPbBr_3$ QDs and SIBS. (b) Representative TEM image shows the spatial distribution of QDs, which are preferentially located at PIB domains. (c) Photo of the QDs/SIBS composites with excellent flexibility and photoluminescence. (d) Stress–strain curves of the QDs/SIBS composite. Reproduced with permission from ref. 48. Copyright 2023 Wiley-VCH. (e) Schematic illustration of the composite composed of PDL-*b*-P3HT-*b*-PDL copolymer and perovskite QDs. (f)–(g) AFM phase image and TEM image of the nanocomposites composed of fibers-like morphology of P3HT and uniformed distributed QDs. Reproduced with permission from ref. 49. Copyright 2023 Elsevier. (h) TEM image of $CsPbBr_3$ perovskite nanowires. (i) TEM image of the SIS polymer filament. (j) Intensity projection of z-stack fluorescence confocal image of the printed nanowire-SIS hybrid filament. (k) TEM image of the printed nanowire-SIS composite filament. (l) Optical images of printed pixel arrays showing polarization-dependent emission multiplexing. Reproduced with permission from ref. 50. Copyright 2019 American Association for the Advancement of Science.

Conjugated triblock copolymer with soft poly(d-decanolactone) (PDL) block and hard poly(3-hexylthiophene) (P3HT) block were integrated with $CsPbBr_3$ QDs to form hybrid structures (Fig. 3e).[49] By selective solvent treatment and tuning PDL branch number, the P3HT blocks showed fiber-like crystalline structure that led to improved self-aggregation of perovskite QDs, increased grain size, and optimized interfaces between P3HT and perovskite QDs (Fig. 3f and g). The PDL blocks also provided mechanical flexibility, making it possible for a stretchable photosynaptic transistor that operated with ultralow energy consumption.

Spatial control or alignment of perovskite nanostructures inside a BCP matrix can also be achieved by extrusion-based 3D printing. For instance, Zhou *et al.*[50] demonstrated 3D printing with nanocomposites composed of $CsPbX_3$ nanowires and polystyrene-polyisoprene-polystyrene block copolymer (SIS) block copolymer (Fig. 3h and i). Alignment of perovskite nanowires in the soft matrix can be achieved with different printing paths (Fig. 3j and k). Such alignment resulted in soft optical materials with highly anisotropic and polarized absorption and emission (Fig. 3l). Optical devices based on such nanocomposites including optical storage and full-color displays were also demonstrated.

2.2 BCP micelles/stars as template for the synthesis of perovskite NCs

Besides the capability to self-assemble into microphase-separated morphology in the solid state, another interesting feature of BCP is that they can assemble into micelles of

different geometries in selective solvents. For instance, amphiphilic BCPs with hydrophilic and hydrophobic blocks tend to assemble into spherical micelles consisting of a hydrophobic core and hydrophilic shell in aqueous solution to minimize the interfacial free energy. Such micelles can be used as the template or nanoreactor for perovskite NCs synthesis.[51]

For instance, PS-*b*-P2VP micelles were used as the template for $MAPbX_3$ NCs synthesis (Fig. 4a and b).[52] Due to the encapsulation by polymer shell, the perovskite NCs showed enhanced stability against water degradation and halide ion migration. Thin films comprising these NCs exhibited a more than 15-fold increase in lifespan in comparison to pristine NCs in ambient conditions and had good stability even when immersed in water (Fig. 4c). In a follow-up study,[53] $MAPbBr_3$ perovskite QDs were synthesized using PS-*b*-P2VP micelles as nanoreactor and the length of PS block on Förster resonance energy transfer (FRET) efficiency was studied. Longer PS block resulted in higher stability but hindered the dipole–dipole interaction between the QDs acceptor and 2D $CsPbBr_3$ nanoplatelets donors. It was also demonstrated that the combination of BCP micelle and organic ligands during perovskite NCs formation process led to enhanced optical stability.[54] The organic ligand helped to passivate the QDs surface inside the micelles and excessive ligands formed a lamellar bilayer structure surrounding the micellar-encapsulated perovskite QDs.

Using a similar strategy, POSS-PMMA-*b*-PDMAEMA (POSS: polyhedral oligomeric silsesquioxane, PDMAEMA: poly 2-(dimethylamino)ethyl methacrylate) copolymer micelles were used for the preparation of $CsPbBr_3$ QDs.[57] The hydrophobic POSS and PMMA blocks provided excellent barrier properties against moisture and led to enhanced stability of the perovskite NCs. Beyond simple spherical or cubic shapes, perovskite NCs with other shapes can also be synthesized by the block copolymer micelle template method. For instance, nanoplates and rod-like $MAPbBr_3$ NCs were demonstrated by controlling the PS-*b*-P2VP block copolymer micelles formation and their disassembly.[58]

Chiral perovskite NCs were also synthesized by using block copolymer inverse micelles as the template. PS-*b*-P2VP was mixed with racemic DL-alanine (DL-ala) through hydrogen bonding and then used as the template for $MAPbBr_3$ NC synthesis (Fig. 4d and e).[55] The selective occupation of perovskite precursors within chiral micellar cores resulted in chirality transfer to the electronic states of the perovskite NCs, which led to a

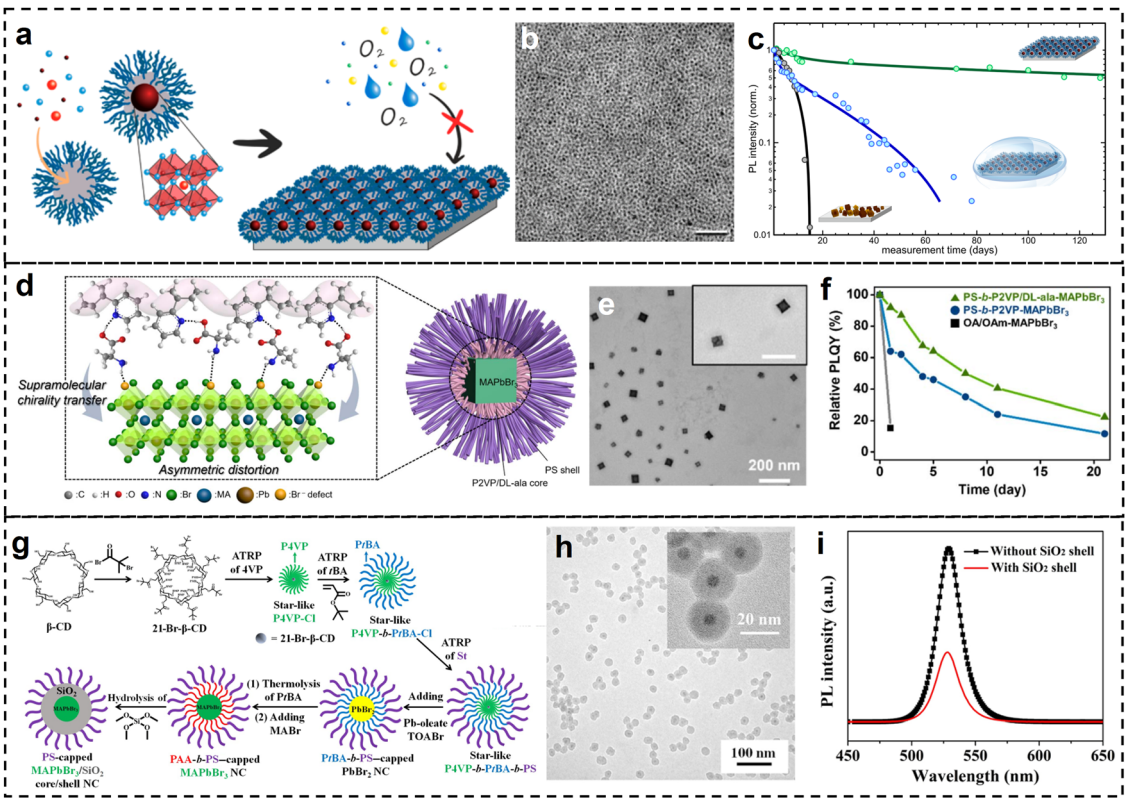

Fig. 4 (a) Schematic representation of the preparation of perovskite NCs from PS-*b*-P2VP copolymer micelles and their enhanced stability. (b) TEM image of the prepared $MAPbX_3$ NCs. (c) Temporal development of PL intensity of the hybrid perovskite NC films in ambient conditions and under water, compared with pristine regular MAPI NCs. Reproduced with permission from ref. 52. Copyright 2019 American Chemical Society. (d) Structure of the chiral PS-*b*-P2VP/DL-ala BCP micelle encapsulated $MAPbBr_3$ NCs. (e) TEM image of the prepared $MAPbBr_3$ NCs. (f) Thermal stabilities of the PS-*b*-P2VP/DL-ala micelle-encapsulated $MAPbBr_3$ NCs (green). The OA/OAm-capped $MAPbBr_3$ NCs (black) and the PS-*b*-P2VP micelle-encapsulated $MAPbBr_3$ NCs (blue) were used as controls. Reproduced with permission from ref. 55. Copyright 2023 Royal Society of Chemistry. (g) Stepwise representation of the synthetic route to PS-capped $MAPbBr_3/SiO_2$ core/shell NCs. (h) TEM images of PEO-capped $MAPbBr_3/SiO_2$ core/shell NCs. (i) PL spectra of $MAPbBr_3$ core NC before and after the SiO_2 shell coating dispersed in toluene. Reproduced with permission from ref. 56. Copyright 2019 American Association for the Advancement of Science.

high chiroptical response with an anisotropy factor of -2.0×10^{-4}. The surface encapsulation also led to enhanced PL stability (Fig. 4f) In another report,[59] $CsPbX_3$ and $FAPbX_3$ NCs were synthesized from PAA-*b*-PS micelle as the template. Functional additive organic molecules were also incorporated into the hybrid structure to enhance the nanocrystal stability against polar solvents and high flux irradiation. Halide exchange process of the hybrid perovskite NCs was possible when the PS block was swollen in a good solvent.

Besides spherical micelles formed by self-assembly of BCP, star-like BCPs have a similar morphology but chemically bonded structure, which can also be used as the molecular template for perovskite QDs synthesis and functionalization. For instance, by using sequential atom transfer radical polymerization (ATRP), star-like P4VP-*b*-P*t*BA-*b*-PS BCPs were synthesized and used as the templates for $MaPbBr_3$ NC synthesis in the P4VP core region (Fig. 4g).[56] Subsequent thermolysis of PtBA and hydrolysis of tetramethyl orthosilicate resulted in the formation of SiO_2 shell on the surface of $MAPbBr_3$ NC. The size and shell thickness of such hybrid perovskites NCs can be tuned (Fig. 4h). Such hybrid perovskites NCs showed enhanced PL stability due to the passivation effects of the SiO_2 shell and chemically-bonded polymer ligands on the surface (Fig. 4i).

Using a similar strategy, $CsPbBr_3$ QDs were synthesized by using star-like PS-*b*-PAA as the nanoreactors.[60] In addition, hollow perovskite NCs with a PS core were also prepared with star-like PS-*b*-PAA-*b*-PS as the template.[61] The presence of the PS core caused a blue shift of PL spectra which can be adjusted by controlling the PS core size. In another report,[62] star-like PAA-*b*-P3HT BCP was used as the template for $CsPbBr_3$ QDs synthesis. The Lewis acid–base interaction between P3HT ligands and the QDs resulted in efficient charge carrier separation compared with the physical mixture of P3HT and perovskite QDs. Similarly, star-like PHEMA-*g*-(PAA-*b*-PS) block copolymers were used as the template for preparation of $CsPbBr_3$ QDs,[63] which showed enhanced stability against UV, moisture, heat, and water, due to permanently ligated hydrophobic PS on the surface.

2.3 BCP as macromolecular ligands for perovskite NCs

BCPs can also be used as the macromolecular ligands for perovskite NCs, which have the effect of enhanced stability and dispersion in different solvents. Compared with conventional short organic ligands for perovskite NCs, the polymeric ligands have more flexibility in chemical composition and introduce new functionalities. For instance, PS-*b*-PAA was introduced during the formation of $CsPbBr_3$ QDs,[64] and the

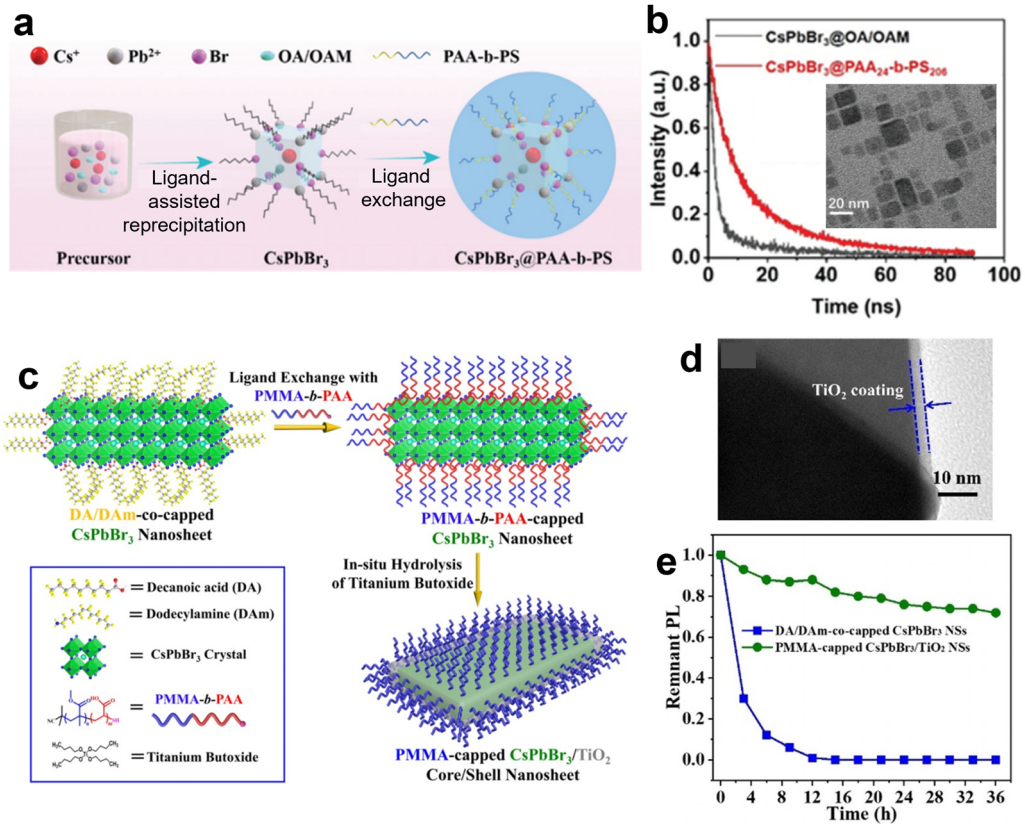

Fig. 5 (a) Schematic of the process for the formation of $CsPbBr_3$@PAA-*b*-PS structure. (b) Time-resolved PL of the NCs with copolymer ligands and short organic ligands. Inset is the TEM image of the NCs with copolymer ligands. Reproduced with permission from ref. 64. Copyright 2022 Royal Society of Chemistry. (c) Schematic illustration of crafting $CsPbBr_3/TiO_2$ core/shell NS with chemically bonded PMMA ligands *via* a two-step process. (d) TEM image of the PMMA-capped $CsPbBr_3/TiO_2$ core/shell NSs. (e) PL thermal stability of the PMMA-capped $CsPbBr_3/TiO_2$ NS and its control sample at 70 °C. Reproduced with permission from ref. 65. Copyright 2021 Wiley-VCH.

amphiphilic copolymers acted as ligands for the perovskite QDs (Fig. 5a). Enhanced stability and photoluminescence quantum yields were achieved compared with conventional QDs with short organic ligands (Fig. 5b).

In another study,[66] PS-*b*-PEO copolymer was used as the polymer ligands for $MAPbBr_3$ QDs synthesis. Such perovskite QDs can be dispersed well individually or self-assembled into well-defined vesicular nanostructures with high photoluminescence quantum yields. The high stability in water enabled its application in cell imaging. PBMA-*b*-PSBMA and PBMA-*b*-PMPC (PBMA: poly(*n*-Butyl methacrylate), PSBMA: poly(sulfobetaine methacrylate), PMPC: poly(2-methacryloyloxyethyl phosphorylcholine)) zwitterionic copolymers were used as polymer ligands during $CsPbX_3$ NCs synthesis.[67] The prepared perovskite NCs with BCP ligands were found to disperse and maintain their fluorescence in a range of polar organic solvents and enable direct integration into optically transparent nanocomposite thin films with high perovskite content.

Perovskite NCs with other geometries can also be synthesized with BCP as the polymeric ligands. For instance, PS-*b*-P4VP was used as the polymer ligands for $CsPbBr_3$ nanowires.[68] The surface-modified nanowires showed enhanced photoluminescent emission and good colloidal stability against water. Such nanowires were further assembled into highly aligned monolayer by the Langmuir–Blodgett technique and exhibited anisotropic optical properties.

Furthermore, the BCP ligands can also be used as the intermediate for the synthesis of inorganic shell on the surface of perovskite NCs. For instance, He *et al.* demonstrated the synthesis of perovskite nanosheets protected by TiO_2 shell and hydrophobic PMMA brushes (Fig. 5c–e).[65] Specifically, PMMA-*b*-PAA chains were anchored onto the nanosheet surface as multidentate ligands by a ligand exchange process. Then, *in situ* hydrolysis of mixed titanium butoxide was catalyzed by a trace amount of moisture and the -COOH groups of the PAA segments, generating a layer of TiO_2 precisely on the perovskite surface with PAA blocks. The dual-shelled perovskite showed excellent stability against moisture, polar solvents, aliphatic amine, *etc.*

2.4 BCP encapsulation of perovskite NCs into composite particles

When BCPs and perovskite NCs are placed in a selective solvent or the BCP is polymerized with the presence of perovskite NCs, it is possible to form composite particles with a BCP shell or matrix and multiple perovskite NCs encapsulated in the interior. For instance, $CsPbBr_3$ NCs were encapsulated in polymer capsules made of PS-*b*-PAA copolymers by using selective solvents (Fig. 6a and b).[69] Such copolymer capsule encapsulated perovskite NCs showed an high photoluminescence quantum yield ($\sim$60%) that was preserved over two years in water (Fig. 6c). Such capsules can be used as photoluminescent probes for cell imaging at a very low dose so that no significant cell toxicity was found.

Perovskite QDs can be used as both luminescence centers and photocatalysts to prepare organic–inorganic nanohybrid assemblies. For instance, Shi *et al.*[70] used perfluorooctanoic acid-modified $CsPbBr_3$ QDs as the photocatalyst to induce *in situ* self-assembly of POEGMA-*b*-PFOEMA (POEGMA: poly(poly(ethylene glycol) monomethyl ether methacrylate), PFOEMA: poly(perfluorooctyl)ethyl methacrylate) nanoparticles by RAFT polymerization in which the POEGMA worked as the macro chain transfer agent and the FOEMA as the monomer (Fig. 6d). Modulation of the block length led to the transition from nanorods to spindle-like nanoassemblies (Fig. 6e and f) and these hybrid nanoparticles showed high fluorescence and enhanced stability.

In another report, $CsPbBr_3$ QDs were encapsulated by PEG-*b*-PCL (PCL: polycaprolactone) copolymers and the hybrid structures showed improved water stability and biocompatibility (Fig. 6g and h),[71] Such structures were used for H_2S gas sensing due to the quenching effect of H_2S to the PL intensity of perovskite QDs. Similarly, Colloidal $CsPbBr_3$ QDs were encapsulated by amphiphilic PEO-PPO-PEO triblock copolymer,[72] such hybrid nanospheres showed good water dispersity and stable photoluminescence.

2.5 BCP/perovskite bulk composite films

When BCP is introduced during the fabrication/crystallization of bulk perovskite films, it is possible to form BCP/perovskite bulk composite films when there is strong and/or selective interaction between BCP and crystalline perovskite. Conjugated BCP can be mixed with perovskite precursors to prepare hybrid semiconductors for high-performance solar cell fabrication. For instance, Sun *et al.* integrated PBDB-T-*b*-PTY6 (Fig. 7a) with lead halide perovskites into bulk heterointerfaces for solar cell devices (Fig. 7b).[73] The incorporation of BCP did not obviously change the crystalline structure of the perovskites because it was mainly located at the surface and grain boundaries. The BCP efficiently passivated the grain boundaries and resulted in smooth and uniform hybrid organic/perovskite film (Fig. 7c and d), which facilitated the carriers extracting and transporting process. Moreover, the hydrophobic PBDB-T-*b*-PTY6 also acted as a barrier for moisture invasion, providing enhanced operational and storage stability.

In another report, Zong *et al.* incorporated PEO-PPO-PEO with perovskite precursors to fabricate hybrid $MAPbI_3$ perovskite films for solar cell devices (Fig. 7e).[74] The triblock copolymer acted as heterogeneous nucleation sites during the perovskite crystallization process, as a result, smaller grain size and fewer surface defects are detected (Fig. 7f), which led to solar cells with improved performance and environmental stability. Similarly, PEO-PPO-PEO was integrated with $MA_{0.7}FA_{0.3}PbI_3$ and the hybrid film was used to fabricate solar cells.[75] The copolymer preferentially located at the grain boundaries and suppressed the decomposition of the organic species. The hydrophobic PPO block also acted as the moisture barrier and increased the device stability. Li *et al.* used a two-step spin-coating process with $PbAc_2{\cdot}3H_2O$ as the lead source and PS-*b*-P2VP to fabricate hybrid perovskite films with enhanced stability.[76] The $PbAc_2{\cdot}3H_2O$ was selected for its larger molecular volume, which could alleviate the volume expansion during the perovskite crystallization process, resulting in a dense and uniform film with higher PLQY.

The integration of soft copolymers with perovskite into bulk composites also enables the fabrication of flexible optical or photonic devices. For instance, PU-PDMS copolymers containing

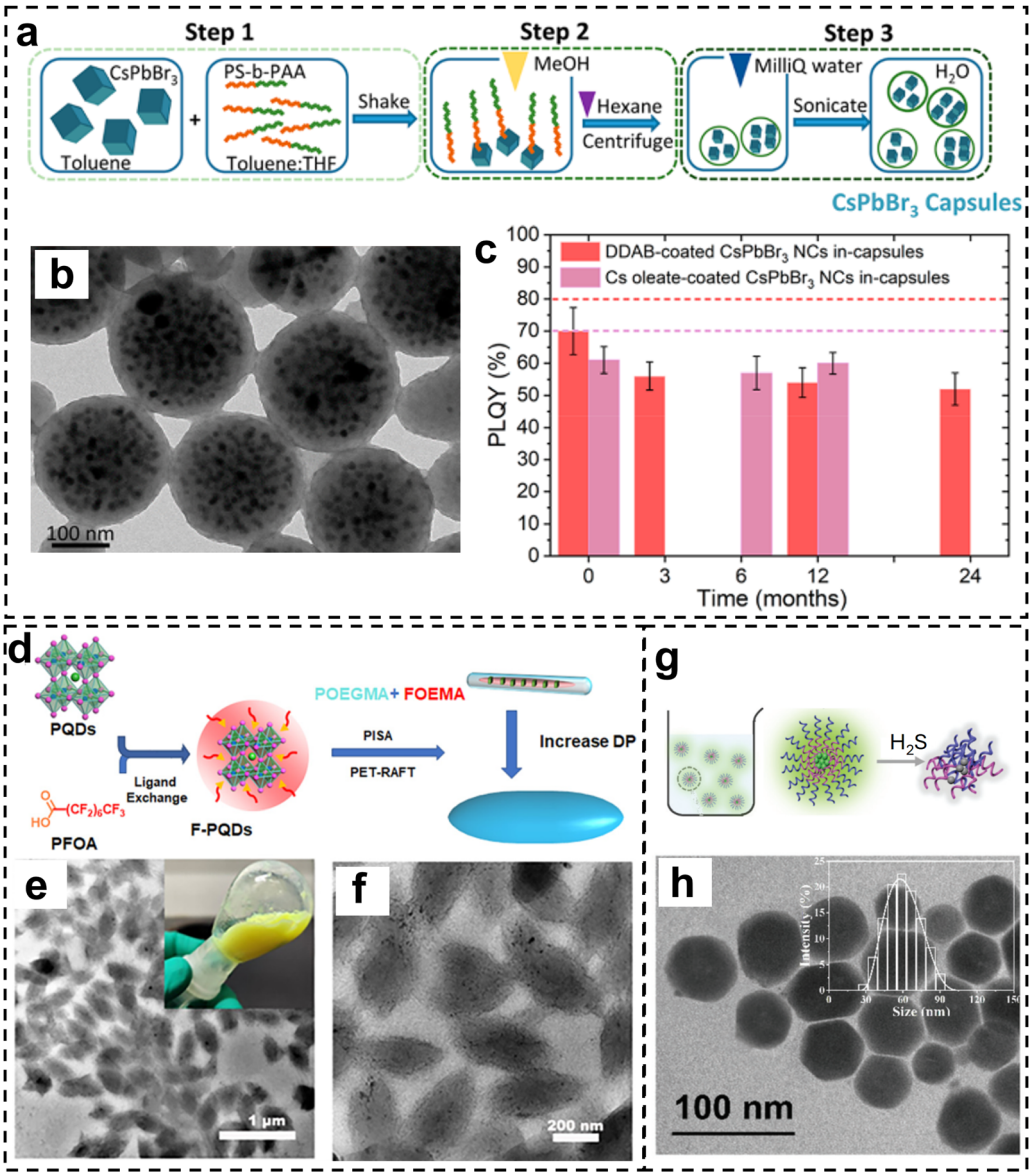

Fig. 6 (a) Schematic illustration of the process for the fabrication of the copolymer capsules embedding the $CsPbBr_3$ NCs. (b) TEM image of the capsules with $CsPbBr_3$ NCs inside. (c) PLQY tracking of capsules dispersed in water over months. Reproduced with permission from ref. 69. Copyright 2022 American Chemical Society. (d) Schematic of the ligand exchange strategy of PQDs and the PISA process based on PET-RAFT polymerization. (e) and (f) TEM images of the hybrid particles with $CsPbBr_3$ QDs embedded inside. Reproduced with permission from ref. 70. Copyright 2024 Royal Society of Chemistry. (g) Schematic of the preparation of polymer micelles encapsulated QDs and the H2S-responsive behavior. (h) TEM image of the hybrid structures. Reproduced with permission from ref. 71. Copyright 2021 Royal Society of Chemistry.

Lewis-base functional groups and elastomer chains were introduced into MHP perovskites (Fig. 7g and h).[77] The soft copolymers have multiple effects including controlled crystal growth, defect passivation, protection against moisture, mechanical energy dissipation, and self-recoverability. Solar cell devices with the hybrid perovskite films showed enhanced operational stability against illumination and elevated temperature (Fig. 7i).

Stretchable luminescent nanocomposites with MHP emitters were fabricated by a two-step process (Fig. 7j).[78] P2VP-*b*-PDMS copolymer was first introduced to the crystallization process of $PEA_2(FAPbBr_3)_2PbBr_4$, and then the hybrid material was added to a PDMS matrix and cured. The BCP promoted the crystallization of the MHP as nanocrystals with an average diameter of 5.9 nm. Moreover, the copolymer enabled uniform dispersion of the perovskite NCs in the PDMS matrix, so that the nanocomposites showed stable PL emission upon repetitive stretching, and excellent environmental stability (Fig. 7k and l). Similarly, SEBS was used as the polymer matrix for $CsPbBr_3$ QDs, and such nanocomposites showed enhanced PL stability against water and oxygen.[28] The alkyl chains in the SEBS created a more compatible QDs-polymer interface due to the similar chemical structure with the organic ligands on QDs. Polyfluorene-*block*-poly(*n*-Butyl acrylate) (PF-*b*-PBA) copolymer was blended with $CsPbBr_3$ NCs,[79] and the composite was used to fabricate

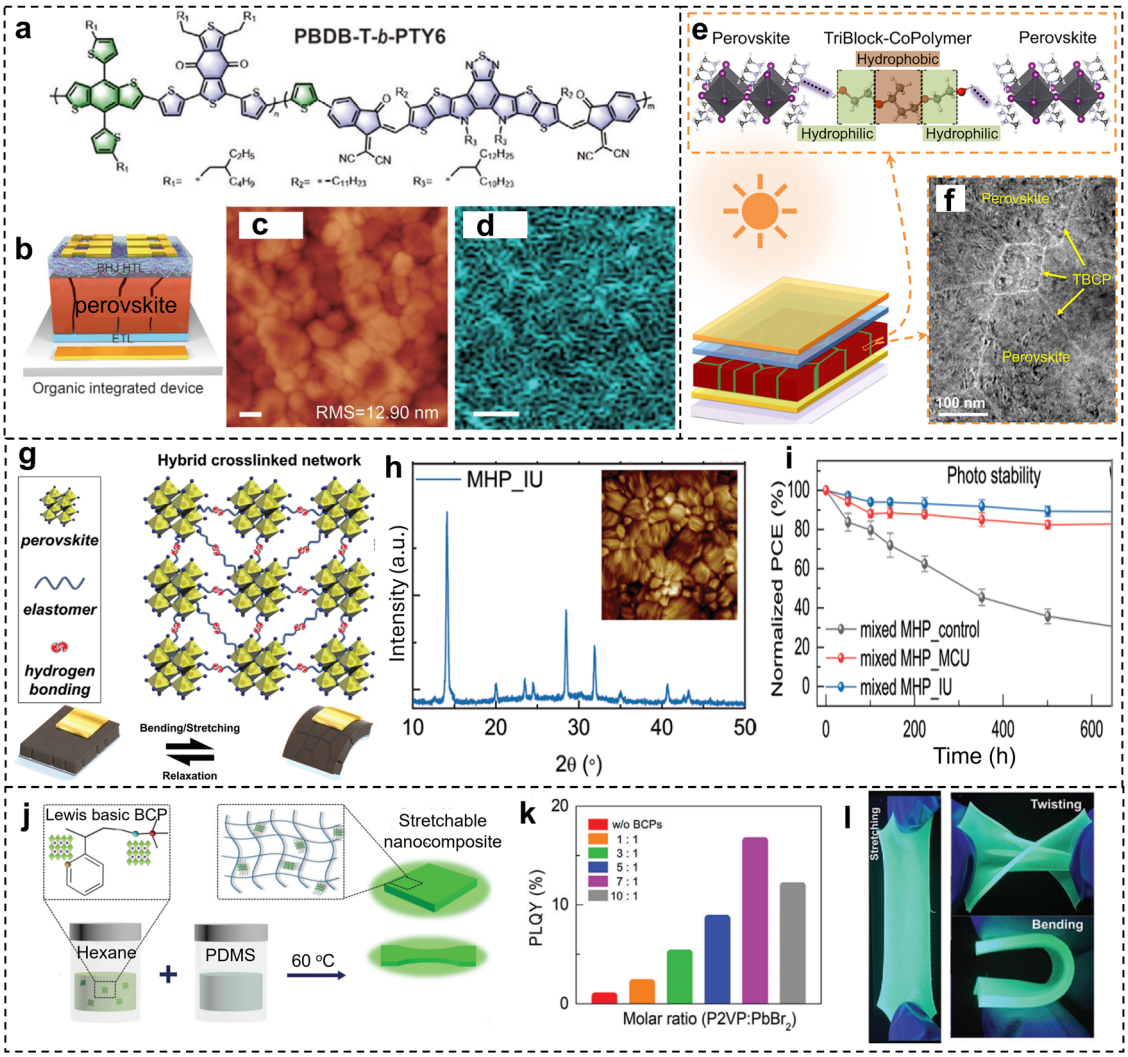

Fig. 7 (a) Chemical structure of the conjugated BCP used for forming hybrid perovskite structures. (b) Solar cell device with the BCP/perovskite heterointerfaces. (c) and (d) AFM image and confocal PL mapping of the hybrid perovskite film. Scale bars are 100 nm. Reproduced with permission from ref. 73. Copyright 2023 Wiley-VCH. (e) Schematic of the interaction between PEO-PPO-PEO copolymer and $MAPbI_3$ perovskite, as well as the solar cell device. (f) TEM image of the hybrid $MAPbI_3$ perovskite film. Reproduced with permission from ref. 74. Copyright 2018 Cell Press. (g) Schematic illustration of hybrid network composed of MHP and PU-PDMS copolymer and its energy-dissipation and self-recovery mechanism. (h) XRD spectrum of the hybrid MPH film with PU-PDMS copolymer, inset is the AFM image of the sample. (i) PCE evolution of solar cell devices with time under light illumination (90 ± 10 mW cm^{-2}). Reproduced with permission from ref. 77. Copyright 2022 Wiley-VCH. (j) Schematic of the sequential fabrication process for the stretchable composites composed of $PEA_2(FAPbBr_3)_2PbBr_4$ NPs with P2VP-*b*-PDMS and PDMS matrix. (k) PL quantum yield of the perovskite composites fabricated with different ratios of the copolymer and PbBr2 precursor. (l) Photos of the composites under stretching, twisting, and bending. Reproduced with permission from ref. 78. Copyright 2024 Wiley-VCH.

composite fiber using electrospinning. The conjugated PF block served as the donor in the double fluorescence combination so the color of the electrospun structures can be conveniently varied by changing the BCP/QDs ratio. The soft PBA block, on the other hand, enabled good stretchability of the composite fibers.

3. Applications of perovskite–BCP hybrid structures

3.1 Solar cell

The fundamental structure of a perovskite solar cell consists of metal anode, hole transport layer, light-absorbing perovskite layer, electron transport layer and transparent cathode.[80] Typically, the perovskite layer is in polycrystalline form fabricated by solution-based procedures,[81] which has inevitable defects ranging from point defects to grain boundaries that negatively affect the charge transport property of solar cells.[82,83] Generally, grain boundaries are most susceptible to degradation as they can trap impurities including solvent and moisture during perovskite thin film processing. The dangling bonds along the grain boundaries also lead to diffusion of small molecules and ions. The integration of BCPs during perovskite layer fabrication has been utilized to address this issue.

The incorporation of BCP can enhance the operational stability of the perovskite layer in solar cells. This has been

demonstrated by perovskite solar cells (PSC) with a perovskite layer mixed with PEO-*b*-PPO-*b*-PEO,[74,75] which showed over 20% power conversion efficiency (PCE). The hydrophilic PEO blocks interact with unbonded cations of the perovskite and thus build a network functionalizing all grain boundaries throughout the thin film. This network composed of hydrophilic PEO and hydrophobic PPO simultaneously passivates surface defects and repels moisture. PSC with hybrid PU-PDMS/perovskite layer showed PCE of 22.6% and enhanced operational stability.[77] An energy dissipation network was formed by PU-PDMS due to the intermolecular hydrogen bonds, making the solar cell more resistant to mechanical stress. The reversable nature of hydrogen bond reformation leads to self-healing effect so that cracks can be repaired at elevated temperature. BCPs can also participate in the carrier transfer process beyond acting as passivating and encapsulating agents. For instance, PSC with a PBDB-T-*b*-PTY6/perovskite heterointerface achieved a high power conversion efficiency (PCE) of 24.1%.[73] This improvement was attributed to an additional energy cascade, reflecting a type II energy level alignment introduced by the conjugated and hydrophobic BCP, which facilitates exciton dissociation while preventing moisture diffusion.

The full potential of using BCP-perovskite nanocomposite as the active layer for solar cells has not been achieved yet and there is still much room for improvement. Conjuated BCPs with both donor and acceptor behavior that can also form vertically aligned channel with perovskite NCs inside such channels present an ideal active layer for solar cells. Such a structure would enable almost flawless charge transport in combination with efficient charge separation at the perovskite NCs.[84] Experimental demonstration of such a structure has not been reported yet. What's more, bandgap alignment of the BCP-perovskite nanocomposite with other components of the solar cels is critical to avoid back energy transfer and maximize light absorption.[85]

3.2 LED

The working principle of a light-emitting diode is the radiative recombination of injected electrons and holes. LEDs have an identical device structure as solar cell since they both involve the excitation and recombination of electron–hole pairs in a semiconductor but utilizing the material in a reverse manner.[86,87] Perovskites, especially their QDs, are being extensively studied for next-generation LEDs.[88,89] Perovskite–BCP hybrid structures have been investigated for LED applications due to the potential to eliminate surface defects and protect ionic perovskite from the external environment. PS-*b*-PAA is one of the frequently used BCP for this purpose.[60,61,64] Color tuning of perovskite–BCP LEDs can be achieved by either halide anion exchange reaction[59] or changing the perovskite QDs/polymer ratios.[79] Specifically, anion exchange can be achieved by exposing the PS-*b*-PAA encapsulated perovskite QDs in a selective solvent such as toluene, so that the swollen PS chains allows the ion diffusion and halide exchange. The incorporation of BCPs with a conjugated block can also lead to color tuning without halide exchange reaction. For instance, polyfluorene blocks on a BCP not only exhibit hole transport properties but also function as blue-emitting moieties. By leveraging the double fluorescence combination, the emission color of the perovskite–BCP composite can be adjusted by varying the ratios of QDs to BCP.

Beyond their role of encapsulation and passivation of perovskite crystals, the long-range order achieved from microphase separation of BCPs can potentially lead to alignment of perovskite NCs for optimized charge transport in LED devices.[29] For instance, if one block of the BCP form vertical cylinders with high density of aligned perovskite NCs inside, such composite structure would be ideal active layer or a color-conversion layer for LED. In such a case, the nanoconfinement leads to enhanced electronic coupling between perovskite NCs and avoids charge transport imbalance, the BCP channels also prevent electrical decoupling from occurring within or between perovskite NCs.[90]

Moreover, BCPs are known to be able to form photonic crystal structures because of the well-defined microphase separated morphology and the refractive index difference between the blocks. Such tunable photonic band gaps and structural colors of BCP matrices can also be utilized to further increase the functionality and optical performance of BCP-perovskite nanocomposites in LED applications, although this remains to be experimentally demonstrated.

3.3 Photodetector

Perovskite as a photoactive material can generate electron–hole pairs when excited by incident light of proper wavelength, so that it can be readily used for photodetection. By incorporating BCP in the perovskite layer, enhanced device stability or anisotropic photodetection induced by nanopatterning can be achieved[44,47] Amphiphilic BCPs are particularly suitable for this purpose as they can passivate the perovskite surface through hydrogen bonding or other interactions, and at the same time, provide hydrophobic protection layer against small molecules.[91] The combination of nanoimprinting and BCP lithography led to the fabrication of sub-30 nm 1D nanopatterns of 2D perovskites over a large area with anisotropic photocurrent generation. Furthermore, the tunable microphase-separated morphology of BCP/perovskite hybrid structures can also be used for artificial visual reception. For instance, a retina-inspired phototransistor based on PS-*b*-P2VP/$MAPbBr_3$ as the photoactive material was demonstrated,[42] the density gradient of perovskite NCs with tunable optical properties emulates the distribution of rod and cone cells in the human retina.

3.4 Chemical and physical sensors

Due to the fluorescence quenching effect of many chemicals and biomolecules to perovskites, the perovskite–BCP hybrid structures can also be used for sensing applications. For instance, sensing of H_2S in physiological conditions was demonstrated by hybrid structures with $CsPbBr_3$ QDs encapsulated by PEG-*b*-PCL.[71] Dopamine can also be detected by perovskite-copolymer microspheres due to the fluorescent quenching of perovskite by dopamine in its oxidized state.[92] Temperature sensing by perovskite–BCP hybrid structure has also been reported.[93] Hydrogen bonding between 2D perovskite and PEO-*b*-PPO-*b*-PEO resulted in stripping of organic cations from perovskite and a bleached phase, while the

increased temperature can break the hydrogen bonding and recover the colored state. For those applications, in order to have highly consistent sensing performance and long-term stability, it is critical to carefully engineer the BCP-perovskite interface to enable the structural stability of perovskite NCs and easy accessibility to target molecules.

3.5 Bioimaging

By encapsulating perovskite NCs with amphiphilic BCPs, the hybrid nanostructures can diffuse into the cytoplasm of living cells and enable fluorescent bioimaging.[69] The cytotoxicity effect can be reduced by using a low dosage of perovskite NCs.[66] For instance, $CsPbBr_3$ NCs encapsulated by PS-*b*-PAA showed long-term stability in physiological conditions. They can be used for cell imaging at a does as low as 0.3 μg_{Pb} mL^{-1}, which is well below the toxicity threshold for Pb and Cs ions. But it is noted that lead-containing perovskites still pose serious concern in terms of their use in biomedicine.[94] Lead-free perovskites with Cu^{2+}, Sn^{2+}, Bi^{+} or other ions will be better options to be integrated with biocompatible BCPs for biomedical applications.

4. Conclusions and outlook

To sum up, in this Highlight article, we provided a critical overview of the recent progress in creating perovskite–BCP hybrid structures with a focus on the fundamental material aspect and organic–inorganic interfaces. We summarized the representative studies based on the different roles of BCP in the hybrid material system: (1) BCPs act as the nanopattern template for the spatial control and patterning of perovskite NCs; which can be further categorized into (1a) *in situ* formation of perovskite NCs from their precursors inside BCP template; and (1b) directed assembly of perovskite NCs inside BCP matrix. (2) BCP micelles or star-shaped BCPs act as the template for perovskite nanostructure crystallization. (3) BCPs act as the macromolecular ligands for perovskite NCs during their solution synthesis. (4) BCP encapsulation of perovskite NCs into hierarchical composite particles. (5) BCP is incorporated into bulk perovskite and forming bulk composite films. We also briefly discussed the broad applications of perovskite–BCP hybrid structures in various fields. Those different types of perovskite–BCP hybrid structures have their advantages and limitations depending on the specific application. For instance, the use of BCP as template for nanopatterning of perovskites NCs is efficient, scalable, and has low energy cost, but the limitation is that the BCP template is generally electrically insulating, which needs to be selectively removed if direct electrical contact with patterned perovskite is required. The use of BCP micelles or star-shaped BCP act as the template for perovskite nanostructure crystallization enables precise composition and structural control, but the limitations include the requirement of multistep or complex chemical synthesis and its scalability.

Despite the rapid research progress, there are also some major limitations that need to be overcome to achieve the full potential of perovskite–BCP hybrid structures in optics and photonics applications. First, the experimental design and fabrication of perovskite–BCP composites need better guidance from theoretical calculation and multiscale simulation such as density functional theory, molecular dynamics, and coarse-grained modeling, especially in terms of predicting the interfacial structure and microphase-separated morphology. Second, in-depth understanding of the effects of the soft BCP matrix and fillers on the charge carrier properties and optoelectronic characters of perovskite needs to be obtained. Third, precise structural control of the perovskite–BCP composites on molecular or sub-10 nanometer scale is still very challenging to achieve. Fourth, the types of BCPs in terms of their chemical composition and chain architecture that can have synergistic effects with perovskite in their hybrid structures are still limited, more efforts are needed to expand the BCP and perovskite toolbox. Fifth, for bioimaging and biosensing applications, it is necessary to design and synthesize biocompatible BCPs to integrate with perovskite to minimize its cytotoxicity and improve biostability. Last but not least, the costs of both perovskites and block copolymers are relatively high compared with other engineered materials, which can limit their applications in some areas.

To address those challenges, it is important to have interdisciplinary and collaborative efforts from inorganic chemistry, polymer chemistry, materials characterization, multiscale simulation, and device engineering. Moreover, the recent advancement in machine learning and artificial intelligence can also be harnessed to provide guidance and insight to the design and performance prediction of various types of perovskite–BCP hybrid structures. Recent advancement in functional BCPs including those with novel architectures, stimuli-responsive, or self-healing properties remain to be investigated for fabricating functional hybrid structures with perovskites to enable new functionalities. Also, the versatile chemical compositions and microphase-separated morphologies of BCPs combined with tunable chemical structure and optical properties of perovskites have the potential to enable new types of optoelectronic devices with dual or multiple applications. On the other hand, more research efforts are needed to connect the fundamental knowledge in molecular-level structural tuning of BCP-perovskite to device-level performance in practical applications.

Author contributions

W. X. conceived and supervised the study, wrote and revised the draft. N. S. led the literature review and wrote the original draft. J. B. and X. L. contributed to the figures and writing.

Data availability

No primary research results, software or code have been included and no new data were generated or analyzed as part of this Highlight article.

Conflicts of interest

There are no conflicts of interest to declare.

Acknowledgements

This work is supported by the National Science Foundation LEAP grant to W.X. (Award No.: 2213054). We also would like to thank Dr Yitong Dong for the helpful discussion.

References

1 W. Zhang, G. E. Eperon and H. J. Snaith, *Nat. Energy*, 2016, **1**, 16048.
2 Z. Ning, X. Gong, R. Comin, G. Walters, F. Fan, O. Voznyy, E. Yassitepe, A. Buin, S. Hoogland and E. H. Sargent, *Nature*, 2015, **523**, 324–328.
3 C.-Z. Ning, L. Dou and P. Yang, *Nat. Rev. Mater.*, 2017, **2**, 17070.
4 L. Gao, L. N. Quan, F. P. García De Arquer, Y. Zhao, R. Munir, A. Proppe, R. Quintero-Bermudez, C. Zou, Z. Yang, M. I. Saidaminov, O. Voznyy, S. Kinge, Z. Lu, S. O. Kelley, A. Amassian, J. Tang and E. H. Sargent, *Nat. Photonics*, 2020, **14**, 227–233.
5 Y. Jiang, C. Sun, J. Xu, S. Li, M. Cui, X. Fu, Y. Liu, Y. Liu, H. Wan, K. Wei, T. Zhou, W. Zhang, Y. Yang, J. Yang, C. Qin, S. Gao, J. Pan, Y. Liu, S. Hoogland, E. H. Sargent, J. Chen and M. Yuan, *Nature*, 2022, **612**, 679–684.
6 J. Kang and L.-W. Wang, *J. Phys. Chem. Lett.*, 2017, **8**, 489–493.
7 R. E. Brandt, J. R. Poindexter, P. Gorai, R. C. Kurchin, R. L. Z. Hoye, L. Nienhaus, M. W. B. Wilson, J. A. Polizzotti, R. Sereika, R. Žaltauskas, L. C. Lee, J. L. MacManus-Driscoll, M. Bawendi, V. Stevanović and T. Buonassisi, *Chem. Mater.*, 2017, **29**, 4667–4674.
8 F. P. García de Arquer, D. V. Talapin, V. I. Klimov, Y. Arakawa, M. Bayer and E. H. Sargent, *Science*, 2021, **373**, eaaz8541.
9 Q. Zhao, S. Wang, Y.-H. Kim, S. Mondal, Q. Miao, S. Li, D. Liu, M. Wang, Y. Zhai, J. Gao, A. Hazarika and G.-R. Li, *Green Energy Environ.*, 2024, **9**, 949–965.
10 X. Zhou, J. Zhang, X. Tong, Y. Sun, H. Zhang, Y. Min and Y. Qian, *Adv. Opt. Mater.*, 2022, **10**, 2101517.
11 C. Zhu, J. Jin, Z. Wang, Z. Xu, M. C. Folgueras, Y. Jiang, C. B. Uzundal, H. K. D. Le, F. Wang, X. Zheng and P. Yang, *Science*, 2024, **383**, 86–93.
12 T. Ashjari, F. Arabpour Roghabadi and V. Ahmadi, *Appl. Surf. Sci.*, 2020, **510**, 145513.
13 M. Konstantakou, D. Perganti, P. Falaras and T. Stergiopoulos, *Crystals*, 2017, **7**, 291.
14 J.-W. Lee, H.-S. Kim and N.-G. Park, *Acc. Chem. Res.*, 2016, **49**, 311–319.
15 L. Protesescu, S. Yakunin, M. I. Bodnarchuk, F. Krieg, R. Caputo, C. H. Hendon, R. X. Yang, A. Walsh and M. V. Kovalenko, *Nano Lett.*, 2015, **15**, 3692–3696.
16 F. Zhang, H. Zhong, C. Chen, X. Wu, X. Hu, H. Huang, J. Han, B. Zou and Y. Dong, *ACS Nano*, 2015, **9**, 4533–4542.
17 N. Pradhan, *Acc. Chem. Res.*, 2021, **54**, 1200–1208.
18 J. A. Steele, M. Lai, Y. Zhang, Z. Lin, J. Hofkens, M. B. J. Roeffaers and P. Yang, *Acc. Mater. Res.*, 2020, **1**, 3–15.
19 D. Wang, M. Wright, N. K. Elumalai and A. Uddin, *Sol. Energy Mater. Sol. Cells*, 2016, **147**, 255–275.
20 H. Zhang, X. Ren, X. Chen, J. Mao, J. Cheng, Y. Zhao, Y. Liu, J. Milic, W.-J. Yin, M. Grätzel and W. C. H. Choy, *Energy Environ. Sci.*, 2018, **11**, 2253–2262.
21 J. Mao, W. E. I. Sha, H. Zhang, X. Ren, J. Zhuang, V. A. L. Roy, K. S. Wong and W. C. H. Choy, *Adv. Funct. Mater.*, 2017, **27**, 1606525.
22 B. Jeong, H. Han and C. Park, *Adv. Mater.*, 2020, **32**, 2000597.
23 B. Gholipour, G. Adamo, D. Cortecchia, H. N. S. Krishnamoorthy, Muhammad D. Birowosuto, N. I. Zheludev and C. Soci, *Adv. Mater.*, 2017, **29**, 1604268.
24 Z. Wang, T. Yang, Y. Zhang, Q. Ou, H. Lin, Q. Zhang, H. Chen, H. Y. Hoh, B. Jia and Q. Bao, *Adv. Mater.*, 2020, **32**, 2001388.
25 W. Zheng, H. Zhang, X. Wang, X. Zhang, T. Long, H. Wang, W. W. Yu and C. Zhou, *Adv. Opt. Mater.*, 2024, **12**, 2301241.
26 B. Lyu, D. Li, Q. Wang, J. Sun, Q. Xiong, D. Zhang, H. Su and W. C. H. Choy, *Angew. Chem., Int. Ed.*, 2024, **63**, e202408726.
27 C. Cueto, M. Hu, T. P. Russell and T. Emrick, *J. Am. Chem. Soc.*, 2024, **146**, 8189–8197.
28 S. N. Raja, Y. Bekenstein, M. A. Koc, S. Fischer, D. Zhang, L. Lin, R. O. Ritchie, P. Yang and A. P. Alivisatos, *ACS Appl. Mater. Interfaces*, 2016, **8**, 35523–35533.
29 J.-S. Benas, F.-C. Liang, W.-C. Chen, C.-W. Hung, J.-Y. Chen, Y. Zhou, S.-T. Han, R. Borsali and C.-C. Kuo, *Chem. Eng. J.*, 2022, **431**, 133701.
30 S. Kim, H. Lee, H. Han, Y. Park, K. Lee, Y. Kim, G. Zan, J. Lee, D. Kim, J. Kim, B. Jeong, J.-H. Kim and C. Park, *Adv. Opt. Mater.*, 2023, **11**, 2300053.
31 F. S. Bates and G. H. Fredrickson, *Annu. Rev. Phys. Chem.*, 1990, **41**, 525–557.
32 K.-V. Peinemann, V. Abetz and P. F. W. Simon, *Nat. Mater.*, 2007, **6**, 992–996.
33 L. Leibler, *Macromolecules*, 1980, **13**, 1602–1617.
34 M. W. Matsen and F. S. Bates, *Macromolecules*, 1996, **29**, 1091–1098.
35 Y. Mai and A. Eisenberg, *Chem. Soc. Rev.*, 2012, **41**, 5969.
36 Y. Liao, W. Chen and R. Borsali, *Adv. Mater.*, 2017, **29**, 1701645.
37 A. Mathur, S. Khamgaonkar and V. Maheshwari, *Adv. Phys. Res.*, 2023, **2**, 2200088.
38 Y. Li, Y. Lv, Z. Guo, L. Dong, J. Zheng, C. Chai, N. Chen, Y. Lu and C. Chen, *ACS Appl. Mater. Interfaces*, 2018, **10**, 15888–15894.
39 C.-C. Hung, Y.-C. Lin, T.-H. Chuang, Y.-C. Chiang, Y.-C. Chiu, M. Mumtaz, R. Borsali and W.-C. Chen, *ACS Appl. Mater. Interfaces*, 2022, **14**, 30279–30289.
40 W. Yang, L. Fei, F. Gao, W. Liu, H. Xu, L. Yang and Y. Liu, *Chem. Eng. J.*, 2020, **387**, 124180.
41 H. Han, B. Jeong, T. H. Park, W. Cha, S. M. Cho, Y. Kim, H. H. Kim, D. Kim, D. Y. Ryu, W. K. Choi and C. Park, *Adv. Funct. Mater.*, 2019, **29**, 1808193.
42 K. Lee, H. Han, Y. Kim, J. Park, S. Jang, H. Lee, S. W. Lee, H. Kim, Y. Kim, T. Kim, D. Kim, G. Wang and C. Park, *Adv. Funct. Mater.*, 2021, **31**, 2105596.
43 Y.-H. Chang, C.-W. Ku, Y.-H. Zhang, H.-C. Wang and J.-Y. Chen, *Adv. Funct. Mater.*, 2020, **30**, 2000764.
44 Y. Park, H. Han, H. Lee, S. Kim, T. H. Park, J. Jang, G. Kim, Y. Park, J. Lee, D. Kim, J. Kim, Y. S. Jung, B. Jeong and C. Park, *Small*, 2023, **19**, 2300568.
45 Y.-H. Chao, J.-C. Chen, D.-L. Yang, Y.-J. Tseng, C.-H. Hsu and J.-Y. Chen, *Adv. Funct. Mater.*, 2022, **32**, 2112521.
46 H. Han, J. W. Oh, H. Lee, S. Lee, S. Mun, S. Jeon, D. Kim, J. Jang, W. Jiang, T. Kim, B. Jeong, J. Kim, D. Y. Ryu and C. Park, *Adv. Mater.*, 2024, **36**, 2310130.
47 H. Han, J. W. Oh, J. Park, H. Lee, C. Park, S. W. Lee, K. Lee, S. Jeon, S. Kim, Y. Park, B. Jeong, D. Y. Ryu and C. Park, *Adv. Mater. Interfaces*, 2022, **9**, 2200082.
48 C. Tsai, N. Shen, C. Mi, J. Bu, Y. Dong and W. Xu, *Adv. Opt. Mater.*, 2024, **12**, 2302731.
49 W.-C. Chen, Y.-C. Lin, C.-C. Hung, L.-C. Hsu, Y.-S. Wu, C.-L. Liu, C.-C. Kuo and W.-C. Chen, *Mater. Today*, 2023, **70**, 57–70.
50 N. Zhou, Y. Bekenstein, C. N. Eisler, D. Zhang, A. M. Schwartzberg, P. Yang, A. P. Alivisatos and J. A. Lewis, *Sci. Adv.*, 2019, **5**, eaav8141.
51 S. Hou, Y. Guo, Y. Tang and Q. Quan, *ACS Appl. Mater. Interfaces*, 2017, **9**, 18417–18422.
52 V. A. Hintermayr, C. Lampe, M. Löw, J. Roemer, W. Vanderlinden, M. Gramlich, A. X. Böhm, C. Sattler, B. Nickel, T. Lohmüller and A. S. Urban, *Nano Lett.*, 2019, **19**, 4928–4933.
53 M. G. Greiner, A. Singldinger, N. A. Henke, C. Lampe, U. Leo, M. Gramlich and A. S. Urban, *Nano Lett.*, 2022, **22**, 6709–6715.
54 Q. Xue, C. Lampe, T. Naujoks, K. Frank, M. Gramlich, M. Schoger, W. Vanderlinden, P. Reisbeck, B. Nickel, W. Brütting and A. S. Urban, *Adv. Opt. Mater.*, 2022, **10**, 2102791.
55 M. Kim, J. Kim, J. Bang, Y. J. Jang, J. Park and D. H. Kim, *J. Mater. Chem. A*, 2023, **11**, 12876–12884.
56 Y. He, Y. J. Yoon, Y. W. Harn, G. V. Biesold-McGee, S. Liang, C. H. Lin, V. V. Tsukruk, N. Thadhani, Z. Kang and Z. Lin, *Sci. Adv.*, 2019, **5**, eaax4424.
57 A. Pan, L. Yan, X. Ma, Y. Wu, Y. Zhang, G. Zhou and L. He, *J. Alloys Compd.*, 2020, **844**, 156102.
58 Y. Nah, D. Jang and D. Ha Kim, *Chem. Commun.*, 2021, **57**, 1879–1882.
59 M. Imran, B. T. Mai, L. Goldoni, M. Cirignano, H. B. Jalali, F. Di Stasio, T. Pellegrino and L. Manna, *ACS Energy Lett.*, 2021, **6**, 2844–2853.
60 Y. J. Yoon, Y. Chang, S. Zhang, M. Zhang, S. Pan, Y. He, C. H. Lin, S. Yu, Y. Chen, Z. Wang, Y. Ding, J. Jung, N. Thadhani, V. V. Tsukruk, Z. Kang and Z. Lin, *Adv. Mater.*, 2019, **31**, 1901602.
61 S. Pan, Y. Chen, Z. Wang, Y.-W. Harn, J. Yu, A. Wang, M. J. Smith, Z. Li, V. V. Tsukruk, J. Peng and Z. Lin, *Nano Energy*, 2020, **77**, 105043.

62 S. Liang, S. He, M. Zhang, Y. Yan, T. Jin, T. Lian and Z. Lin, *J. Am. Chem. Soc.*, 2022, **144**, 12901–12914.
63 Y. Liu, Z. Wang, S. Liang, Z. Li, M. Zhang, H. Li and Z. Lin, *Nano Lett.*, 2019, **19**, 9019–9028.
64 J. Shen, N. Meng, J. Chen, Y. Zhu, X. Yang, Y. Jia and C. Li, *Chem. Commun.*, 2022, **58**, 4235–4238.
65 Y. He, Y. Liang, S. Liang, Y.-W. Harn, Z. Li, M. Zhang, D. Shen, Z. Li, Y. Yan, X. Pang and Z. Lin, *Angew. Chem., Int. Ed.*, 2021, **60**, 7259–7266.
66 S. Yang, F. Zhang, J. Tai, Y. Li, Y. Yang, H. Wang, J. Zhang, Z. Xie, B. Xu, H. Zhong, K. Liu and B. Yang, *Nanoscale*, 2018, **10**, 5820–5826.
67 C. Cueto, C. Donoghue, K. Bolduc and T. Emrick, *Chem. – Eur. J.*, 2022, **28**, e202200409.
68 H. Liu, M. Siron, M. Gao, D. Lu, Y. Bekenstein, D. Zhang, L. Dou, A. P. Alivisatos and P. Yang, *Nano Res.*, 2020, **13**, 1453–1458.
69 S. K. Avugadda, A. Castelli, B. Dhanabalan, T. Fernandez, N. Silvestri, C. Collantes, D. Baranov, M. Imran, L. Manna, T. Pellegrino and M. P. Arciniegas, *ACS Nano*, 2022, **16**, 13657–13666.
70 B. Shi, W. Hu, S. Li, Z. Xia and C. Lü, *Inorg. Chem. Front.*, 2024, **11**, 2471–2478.
71 F. Luo, S. Li, L. Cui, Y. Zu, Y. Chen, D. Huang, Z. Weng and Z. Lin, *Nanoscale*, 2021, **13**, 14297–14303.
72 S. M. Lee, H. Jung, W. I. Park, Y. Lee, E. Koo and J. Bang, *ChemistrySelect*, 2018, **3**, 11320–11325.
73 J. Sun, B. Li, L. Hu, J. Guo, X. Ling, X. Zhang, C. Zhang, X. Wu, H. Huang, C. Han, X. Liu, Y. Li, S. Huang, T. Wu, J. Yuan and W. Ma, *Adv. Mater.*, 2023, **35**, 2206047.
74 Y. Zong, Y. Zhou, Y. Zhang, Z. Li, L. Zhang, M.-G. Ju, M. Chen, S. Pang, X. C. Zeng and N. P. Padture, *Chem*, 2018, **4**, 1404–1415.
75 C. Wang, Z. Song, D. Zhao, R. A. Awni, C. Li, N. Shrestha, C. Chen, X. Yin, D. Li, R. J. Ellingson, X. Zhao, X. Li and Y. Yan, *Solar RRL*, 2019, **3**, 1900078.
76 C. Li, Y. Chen, F. Liu, K. Liu, X. Li, X. Zhang, H. Zhang, Z. Shi, W. Chen, I. Ahmed, N. Arshid, J. Wang, Z. Sun, S. Xiong and Y. Zhan, *Adv. Mater. Technol.*, 2021, **6**, 2001209.
77 T. Han, Y. Zhao, J. Yoon, J. Y. Woo, E. Cho, W. D. Kim, C. Lee, J. Lee, J. Choi, J. Han, J. Nam, K. Wang, S. Priya, M. Balaban, I. Jeon and Y. Yang, *Adv. Funct. Mater.*, 2022, **32**, 2207142.
78 J. Cheon, J.-M. Park, J. Son, M. Lee, S. Lee, C. Park, H. J. Kim, J.-H. Kim, J. S. Park and B. Jeong, *Adv. Opt. Mater.*, 2024, **12**, 2400407.
79 D.-H. Jiang, S. Kobayashi, C.-C. Jao, Y. Mato, T. Isono, Y.-H. Fang, C.-C. Lin, T. Satoh, S.-H. Tung and C.-C. Kuo, *Polymers*, 2020, **12**, 84.
80 Q. Wang, B. Chen, Y. Liu, Y. Deng, Y. Bai, Q. Dong and J. Huang, *Energy Environ. Sci.*, 2017, **10**, 516–522.
81 K. Wang, D. Yang, C. Wu, M. Sanghadasa and S. Priya, *Prog. Mater. Sci.*, 2019, **106**, 100580.
82 W. Xiang, S. Liu and W. Tress, *Energy Environ. Sci.*, 2021, **14**, 2090–2113.
83 A.-F. Castro-Méndez, J. Hidalgo and J.-P. Correa-Baena, *Adv. Energy Mater.*, 2019, **9**, 1901489.
84 M. C. Scharber and N. S. Sariciftci, *Prog. Polym. Sci.*, 2013, **38**, 1929–1940.
85 K. W. Tan, D. T. Moore, M. Saliba, H. Sai, L. A. Estroff, T. Hanrath, H. J. Snaith and U. Wiesner, *ACS Nano*, 2014, **8**, 4730–4739.
86 Z.-K. Tan, R. S. Moghaddam, M. L. Lai, P. Docampo, R. Higler, F. Deschler, M. Price, A. Sadhanala, L. M. Pazos and D. Credgington, *Nat. Nanotechnol.*, 2014, **9**, 687–692.
87 M. Li, Y. Yang, Z. Kuang, C. Hao, S. Wang, F. Lu, Z. Liu, J. Liu, L. Zeng, Y. Cai, Y. Mao, J. Guo, H. Tian, G. Xing, Y. Cao, C. Ma, N. Wang, Q. Peng, L. Zhu, W. Huang and J. Wang, *Nature*, 2024, **630**, 631–635.
88 S. A. Veldhuis, P. P. Boix, N. Yantara, M. Li, T. C. Sum, N. Mathews and S. G. Mhaisalkar, *Adv. Mater.*, 2016, **28**, 6804–6834.
89 Y. Li, X. Zhang, H. Huang, S. V. Kershaw and A. L. Rogach, *Mater. Today*, 2020, **32**, 204–221.
90 Y. Yang, J. T. Lee, T. Liyanage and R. Sardar, *J. Am. Chem. Soc.*, 2019, **141**, 1526–1536.
91 M. Zhang, Q. Lu, C. Wang, H. Dai, J. He, Z. Mohamed, X. Chen and B. Ge, *Org. Electron.*, 2021, **99**, 106330.
92 J. An, M. Chen, G. Liu, Y. Hu, R. Chen, Y. Lyu, S. Sharma and Y. Liu, *Anal. Bioanal. Chem.*, 2021, **413**, 1739–1747.
93 M. Cinquino, C. T. Prontera, A. Giuri, M. Pugliese, R. Giannuzzi, A. Maggiore, D. Altamura, F. Mariano, G. Gigli, C. Esposito Corcione, C. Giannini, A. Rizzo, L. De Marco and V. Maiorano, *Adv. Mater.*, 2024, **36**, 2307564.
94 J. Li, H.-L. Cao, W.-B. Jiao, Q. Wang, M. Wei, I. Cantone, J. Lü and A. Abate, *Nat. Commun.*, 2020, **11**, 310.

